A New Model for Designing Multiwindow Multipermeability Nonlinear LTCC Inductors

Laili Wang, *Member, IEEE*, Yajie Qiu, *Student Member, IEEE*, Hongliang Wang, *Member, IEEE*, Zhiyuan Hu, *Member, IEEE*, and Yan-Fei Liu, *Fellow, IEEE*

***Abstract*—Nonlinear inductors have wide applications in dc/dc converters. The multiwindow multipermeability nonlinear inductor based on low-temperature co-fired ceramic (LTCC) technology has been proven to have a gradually changing wide-range inductance value curve while requiring no extra dc bias, which makes them suitable in various high-efficiency dc/dc converters. This paper focuses on the design of such a multiwindow multipermeability inductor based on an innovative module. Currently, the design of the LTCC inductors requires complicated simulation when coupling matrices among all the windows are taken into consideration. A simplified model for calculating the inductance value is proposed in this paper to reduce complexity. In the proposed model, the complicated inductance simulation is simplified to calculating inductance of three basic units in a nine-window inductor. By simulating the nine-window inductor, inductance of a rectangle-shaped inductor with any number of evenly distributed windows on it can be calculated. Based on the proposed model, the design guideline of the nonlinear inductor is also summarized. A 16-window two-permeability prototype is presented to demonstrate the design process according to the new model. The complete simulation and the test results are also provided to verify the model. The proposed model correlates with the simulation results very well.**

***Index Terms*—DC–DC power conversion, electromagnetic fields, magnetic devices, packaging, permeability.**

I. Introduction

NONLINEAR inductors are widely used to optimize performances of dc/dc converters in different applications; therefore, it is very important to conduct research studies on nonlinear inductors to improve the performances and investigate new applications. As a special kind of inductor, nonlinear inductors have been discussed and applied in various topologies in literature [1]–[6]. They can be used in the main circuit of buck converters [1], boost converters [2], phase-shift full-bridge converters [3], forward converters [4], and resonant converters [5] to improve their performances. A typical application of nonlinear inductors is to realize soft switching for power switches [1], [4]. In a buck converter, two saturable inductors and an auxiliary switch are applied to realize zero-voltage switching (ZVS) of the main switch and zero-current turn-on and zero-voltage turn-off of the auxiliary switch [1]. To further reduce the power loss, cost, and size, a nonlinear inductor, together with a capacitor, is employed to realize ZVS [6]. This method is further extended to be used in a multiphase application [7]. In a forward converter, a saturable inductor is connected in series with the power switch to form a resonant circuit with the parasitic capacitance of the power switch to realize ZVS [4]. Aside from soft switching, the nonlinear inductors can be also used in resonant converters to realize constant frequency control [8], [9] and to improve the dimming characteristics in lighting applications [10]. In the above literature, the inductors play an important role in improving the performances of the converters. However, there are still three disadvantages of these inductors, hindering their popularity in more applications. First, the inductance changes too fast, forming a sharp inductance curve. Second, in some cases, dc bias is required, causing extra loss and partly offsetting the advantages. Third, the nonlinear inductors are designed with commercial ferrite magnetic cores, which have different temperature expansion coefficients (TECs) with silicon, thus cannot be integrated with silicon directly. To design nonlinear inductors with better characteristics than the conventional ones, multiwindow multipermeability nonlinear inductors based on low-temperature co-fired ceramic (LTCC) technology were proposed in [11]. Multiwindow multipermeability nonlinear inductors have more gradually changing wide-range inductance value curves, which can meet the desired requirements of quite a few power applications. Furthermore, the inductors have distributed air gap and do not need extra dc bias, which make them suitable to improve the efficiency of converters.

LTCC technology has been proven to have the advantage of 3-D high-density integration in many academic papers [12]–[20]. There are also emerging integrated point-of-load products in the industry [22]–[24], showing the promising future of this technology. In LTCC technology, very thin magnetic tapes, capacitor tapes, and ceramic tapes are co-fired together to form an integrated substrate. Since ceramic tapes have nearly the same TEC with silicon, LTCC technology has a high potential to be used to make hybrid integrated dc/dc converters as dc shown in Fig. 1.

The multiwindow multipermeability nonlinear inductors are co-fired with ferrite tapes of different permeability values.

Manuscript received November 2, 2014; revised May 16, 2015; accepted July 3, 2015. Date of publication July 13, 2015; date of current version November 18, 2015. Paper 2014-PEDCC-0705.R1, presented at the 2014 IEEE Applied Power Electronics Conference and Exposition, Fort Worth, TX, USA, March 16–20, and approved for publication in the IEEE TRANSACTIONS ON INDUSTRY APPLICATIONS by the Power Electronic Devices and Components Committee of the IEEE Industry Applications Society.

The authors are with the Department of Electrical and Computer Engineering, Queen's University, Kingston, ON K7L 3N6, Canada (e-mail: lailiwang@gmail.com; yajie.qiu@queensu.ca; hongliang.wang@queensu.ca; zhiyuan.hu@queensu.ca; yanfei.liu@queensu.ca).

Color versions of one or more of the figures in this paper are available online at http://ieeexplore.ieee.org.

Digital Object Identifier 10.1109/TIA.2015.2456060

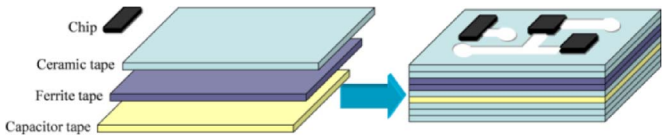

Fig. 1. Structure of an integrated dc/dc converter based on LTCC technology.

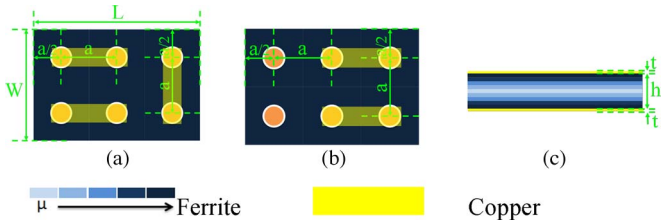

Fig. 2. Six-window multipermeability LTCC nonlinear inductor. (a) Top view. (b) Bottom view. (c) Cross-sectional view.

Fig. 2 shows the structure of a six-window square-shaped multiwindow multipermeability inductor. The windows are evenly distributed on the magnetic core with wires going up and down. By configuring the permeability values and thickness of the cofired ferrite tapes, the desired inductance characteristics can be obtained for different applications. However, the design of such an inductor requires complicated computer-aided finite-element analysis (FEA) simulation (Ansoft 2D is recommended). The iterative process of simulation for determining window size, number of windows, and thickness of the magnetic material of each permeability would be time consuming.

This paper proposes an innovative model to simplify the design of a rectangular-shaped multiwindow multipermeability nonlinear LTCC inductor with evenly distributed windows on it. Section II describes the new model of the nonlinear inductor. Section III demonstrates the design of a multiwindow multipermeability inductor with the proposed model. Section IV shows the prototype and experimental results. Section V concludes this paper.

II. New Model of the Nonlinear Inductors

Multiwindow multipermeability inductors have been proven to show gradual nonlinear inductance characteristic. In addition, this characteristic can be utilized to improve the light and intermediate load efficiency values [11], [12]. However, it is time consuming to design such an inductor only based on a FEA simulation, particularly when the inductor has a large number of windows. As a result, it becomes necessary to derive a new model to simplify the design process. Modeling of inductors has been investigated for a long time, and there have been many literature works discussing about inductance calculation models [10], [25]–[41]. However, the models in these literature works are mainly about conventional inductors and cannot be used to calculate inductance of the new proposed multiwindow multipermeability nonlinear inductors.

As shown in Fig. 2, several parameters should be determined in the design process of the multiwindow multipermeability inductor. They are the permeability values, number of layers with different permeability values, distance between adjacent windows, radius of the windows, and coupling coefficients between

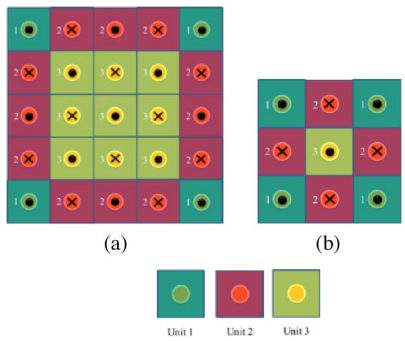

Fig. 3. Twenty-five-window inductor and its units. (a) Twenty-five-window inductor. (b) Nine-window inductor.

windows. To finish the design process by taking all the five parameters into account, complicated FEA simulations should be executed as in [12]. However, the inductance calculation process based on FEA is very time consuming, particularly in the iterative design process. This is mainly because there are coupling coefficients between each window and all the other windows that are fully taken into account during the simulation process. In the design process, the calculation process can be greatly simplified if the couplings between windows are completely neglected, but this will result in big inaccuracy of the calculated inductance value.

To simplify the design of a multiwindow nonlinear inductor while still maintaining the design accuracy, a new model is proposed in this paper. In the new model, coupling between adjacent windows is only taken into consideration, whereas coupling between each other window or between windows that are farther away is neglected. This is because the coupling coefficients between adjacent windows are much larger than the other coupling coefficients. Thus, the windows in the substrate can be classified into three kinds. The first kind of windows is at four corners, which are Unit 1; the second kind is at sides except for those of Unit 1; and the third one is at the inner side of the substrate. Fig. 3 shows a 25-window nonlinear inductor with windows classified into three basic units. The point markers in the windows indicate the current flows from the bottom to the top, whereas the cross markers in the windows indicate the current flows from the top to the bottom. It is shown that, for each window, the neighbor windows on the same row or the same column have opposite current directions whereas the neighbor windows on the oblique lines have the same current direction. Windows with different current directions have the negative coupling coefficients, and vice versa. Among all the windows, there are four Unit 1 windows at four corners of the substrate. In addition, each window has two negative coupling windows and one positive coupling window. Except for the Unit 1 windows, all the windows at four sides belong to Unit 2, which have three negative coupling neighbor windows in a straight line and two positive coupling neighbor windows in oblique lines. The nine windows at the center belong to Unit 3; they have eight neighbor windows, among which are four negative coupling windows in a straight line and four positive coupling windows in oblique lines.

In the new model, the total inductance calculation can be obtained by multiplying the number of each unit and the

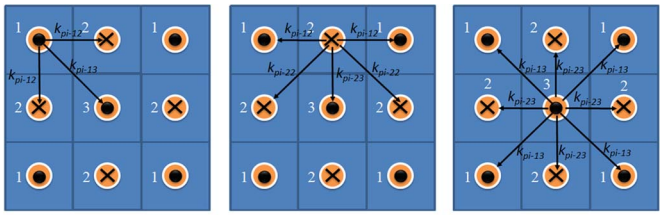

Fig. 4. Coupling coefficients of the three basic units in a nine-window inductor. (a) Unit 1. (b) Unit 2. (c) Unit 3.

inductance of the unit, which is contributed by the window and its coupling neighbor windows. FEA simulation is still a highly efficient way to calculate the inductance of each unit accurately. However, the coupling coefficients between different units should be extracted before the calculation. The minimum simulation substrate that includes all the three units is a nine-window square-shaped inductor. Therefore, the inductance of each unit and their coupling coefficients in any multiwindow nonlinear inductor can be simulated in a nine-window square-shaped inductor that has the same magnetic material characteristics, the same window radius, and the same distance between windows.

In this way, the design of any multiwindow multipermeability nonlinear inductor with windows evenly distributed on the rectangular substrate can be simplified to the inductance calculation of a nine-window multipermeability nonlinear inductor. Thus, there are three steps in the new simplified model. First, the multiple windows on the multipermeability rectangular magnetic substrate are classified into three basic units. Then, the inductance contributed by each unit can be obtained by simulating a nine-window nonlinear inductor, as shown in Fig. 3(b). Finally, the total inductance is obtained by multiplying the inductance of each unit and their corresponding quantities.

To calculate the nonlinear inductance of each unit, incremental flux/current, as shown in (1), should be used. The expressions for inductance calculation of Unit 1, Unit 2, and Unit 3 are shown in (2)–(4)

$$L = \frac{\Delta\Phi}{\Delta I}. \tag{1}$$

As shown in Fig. 4, in each permeability magnetic material pi, the coupling coefficients are classified into four values. The first one is the coupling coefficient between Unit 1 and Unit 2 k_{pi-12}; the second one is the coupling coefficient between Unit 1 and Unit 3 k_{pi-13}; the third one is the coupling coefficient between Unit 2 and Unit 3 k_{pi-23}; and the last one is the coupling coefficient between two Unit 2 cells k_{pi-22}

$$L_{pi-u1}(I) = \frac{\Delta\Phi_{pi}(1 + 2k_{pi-12} + k_{pi-13})}{\Delta I} \tag{2}$$

$$L_{pi-u2}(I) = \frac{\Delta\Phi_{pi}(1 + 2k_{pi-12} + 2k_{pi-22} + k_{pi-23})}{\Delta I} \tag{3}$$

$$L_{pi-u3}(I) = \frac{\Delta\Phi_{pi}(1 + 4k_{pi-13} + 4k_{pi-23})}{\Delta I}. \tag{4}$$

In these three equations, ΔI is the incremental current, and $\Delta\Phi_{pi}$ is the incremental flux generated by an incremental current flowing through each window in magnetic material pi.

Inductance contributed by each permeability magnetic material is expressed by (5). For a multiwindow multipermeability inductor that contains m kinds of permeability, the total inductance can be calculated by adding up the inductances contributed by each unit in each magnetic material, as shown in (6) as follows:

$$L_{pi}(I) = n_1 L_{pi-u1}(I) + n_2 L_{pi-u2}(I) + n_3 L_{pi-u3}(I) \tag{5}$$

$$L(I) = \sum_{i=1}^{m} h_i L_{pi} \tag{6}$$

where h_i is the thickness of each permeability magnetic material. n_1, n_2, and n_3 are the numbers of unit 1, unit 2, and unit 3, respectively.

Direct current resistance (DCR) of the inductor for different configurations is also calculated according to

$$R_{\mathrm{DCR}} = n\frac{\rho h_m}{\pi R^2} + (n-1)\frac{\rho a}{R h_c} \tag{7}$$

where n is the number of windows, ρ is the resistivity of copper, h_m is the thickness of the magnetic core, and h_c is the conductor thickness of the copper on the top and bottom.

To verify the accuracy of the new model, a 25-window two-permeability inductor is simulated with the purpose of comparing the results obtained through the model and simulation. Twenty-five windows are distributed on the substrate evenly. The radius of the window is 0.75 mm, the distance between two windows is 4 mm, whereas the distance between edges and its nearest windows is 2 mm. Two kinds of magnetic materials are selected. One has relative permeability $\mu_r = 50$, and the other one has relative permeability $\mu_r = 200$. As analyzed above, the first step is to classify the windows into three units. The second step is using (2)–(4) to calculate the inductances contributed by each unit, which can be obtained by simulating a nine-window inductor that has the same magnetic materials, radius of windows, and distance between windows. The last step is to calculate the total inductance according to (5). In the comparison, the thickness of the relative permeability $\mu_r = 50$ magnetic material is 2 mm; the thickness of the relative permeability $\mu_r = 200$ magnetic material is 1 mm. Fig. 5 shows the comparison results of the simulation and modeling for $\mu_r = 50$ magnetic material, $\mu_r = 200$ magnetic material, and total inductance when load current increases from 0 to 10 A. The maximum inductance error for $\mu_r = 50$ magnetic material is 4.5%, whereas it is 3.3% for $\mu_r = 200$ magnetic material. For the total inductance, the inductance error is 3.6%. It is shown that the proposed model is very accurate to calculate the inductance value.

III. Design of a Multiwindow Multipermeability Inductor

In this section, a square-shaped 16-window two-permeability inductor is designed based on the proposed model to verify its accuracy. For a general design, the windows' distance a and window radius R should be seen as variables for iterative calculation of the design process. The design guideline is summarized in Fig. 6.

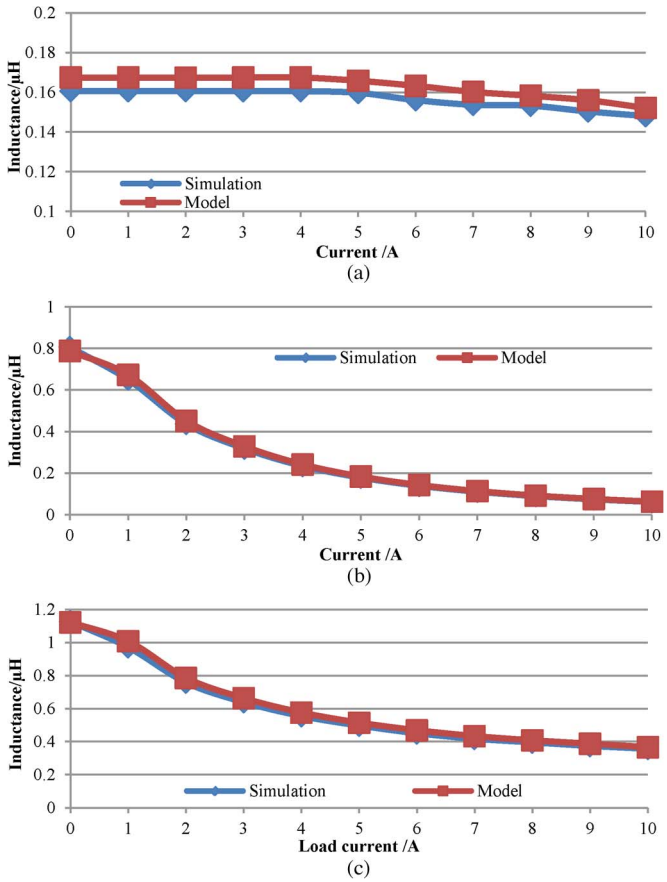

Fig. 5. Inductance curve obtained through the simulation and model. (a) $\mu_r = 50$. (b) $\mu_r = 200$. (c) Total inductance.

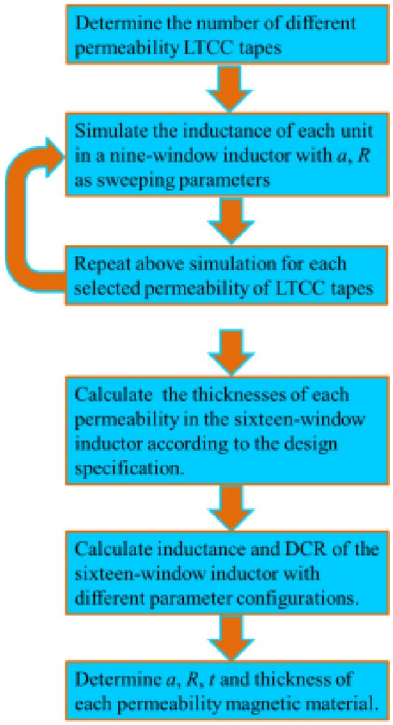

Fig. 6. Flowchart of designing a 16-window nonlinear LTCC inductor.

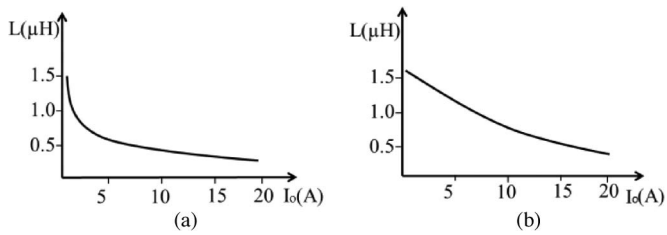

Fig. 7. Inductance of multipermeability inductors. (a) Two-permeability inductor. (b) Five-permeability inductor.

There are big flexibilities when choosing the number of different permeability materials. This depends on how straight the decreasing inductance curve is expected to be configured. The more the number of permeability is, the more linear the inductance curve is. Fig. 7 shows the inductance curves for a two-permeability nine-window inductor and a five-permeability nine-window inductor. The five-permeability inductor has a gradually decreasing inductance curve, whereas the two-permeability inductor has a sharper turning point. In some circumstances such as light load improvement application, higher light load inductance is very beneficial to improve the light load efficiency. To design such a nonlinear inductor, a two-permeability configuration is the simplest way. Therefore, in the new design, two kinds of LTCC ferrite tapes will be used in designing a 3-mm-thick 16-window two-permeability inductor (0.8 μH at 0 A and 0.3 μH at 10 A). Their permeability values are 50 and 200 when operating in a linear region. As described in the last section, the inductance calculation of a multiwindow inductor can be simplified to that of a nine-window inductor; the design of a multiwindow inductor can be thus simplified to an iterative simulation of a nine-window inductor. With radius R and windows' distance a as parameters, 2 nine-window inductors composed of $\mu_r = 50$ ferrite tapes and $\mu_r = 200$ ferrite tapes are simulated. Figs. 8 and 9 show the simulated results of the three basic units with two different permeability values.

As shown in Figs. 8 and 9, both window radius R and window distance a have a significant effect on the inductance value. Smaller R will result in higher inductance. In addition, larger a has the same role but at the cost of higher DCR. It is also shown that R has more impact at light load, whereas a is more effective at full load. For inductors with the same R and a, Unit 1 contributes higher inductance than the other two units in both $\mu_r = 50$ and $\mu_r = 200$ magnetic materials, which means that the windows at four corners contribute higher inductance than others. The square-shaped 16-window inductor shown in Fig. 10 has four Unit 1, eight Unit 2, and four Unit 3. Substituting the number of different units into (5) yields the inductance contributed by each permeability

$$L_{p1}(I) = 4 \times L_{p1-u1}(I) + 8L_{p1-u2}(I) + 4L_{p1-u3}(I) \quad (8)$$

$$L_{p2}(I) = 4 \times L_{p2-u1}(I) + 8L_{p2-u2}(I) + 4L_{p2-u3}(I) \quad (9)$$

where $p1$ is the magnetic material whose relative permeability is 50, and $p2$ is the magnetic material whose permeability is 200.

Inductance contributed by each permeability can be obtained by substituting the data in Figs. 8 and 9 into (8) and (9). The results are shown in Fig. 11.

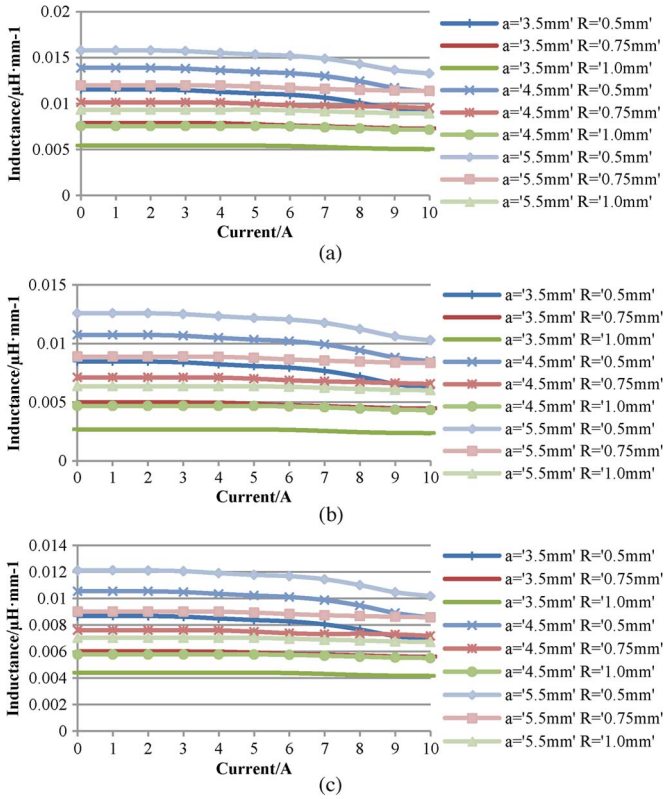

Fig. 8. Inductances contributed by the units ($\mu_r = 50$). (a) Unit 1. (b) Unit 2. (c) Unit 3.

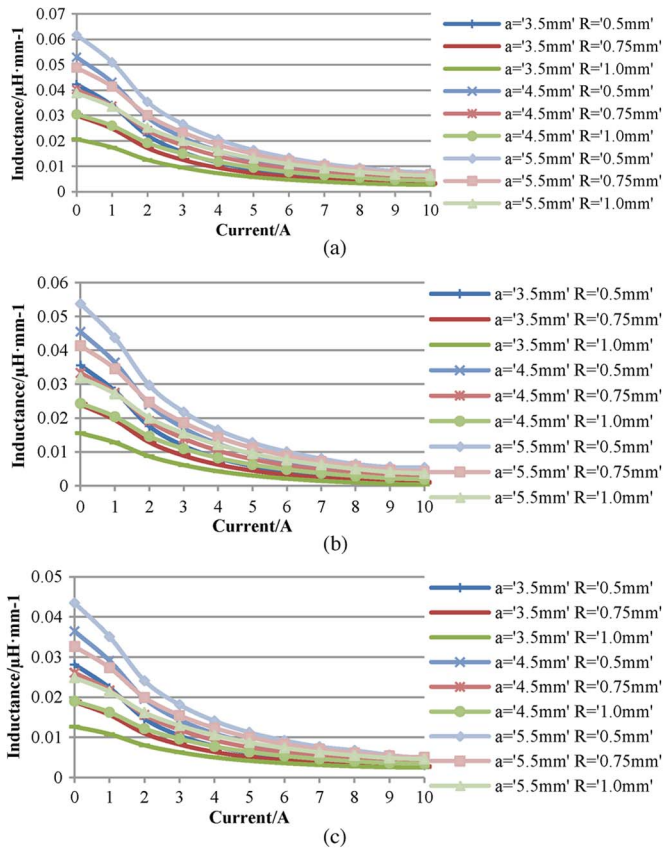

Fig. 9. Inductances contributed by the units ($\mu_r = 200$). (a) Unit 1. (b) Unit 2. (c) Unit 3.

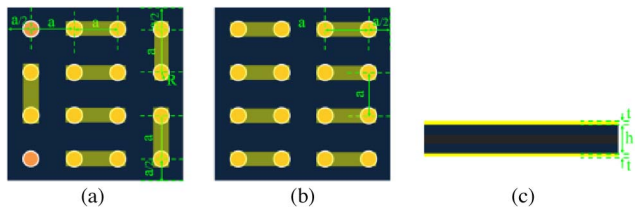

Fig. 10. Top and bottom views of the 16-window two-permeability inductor. (a) Top view. (b) Bottom view. (c) Side view.

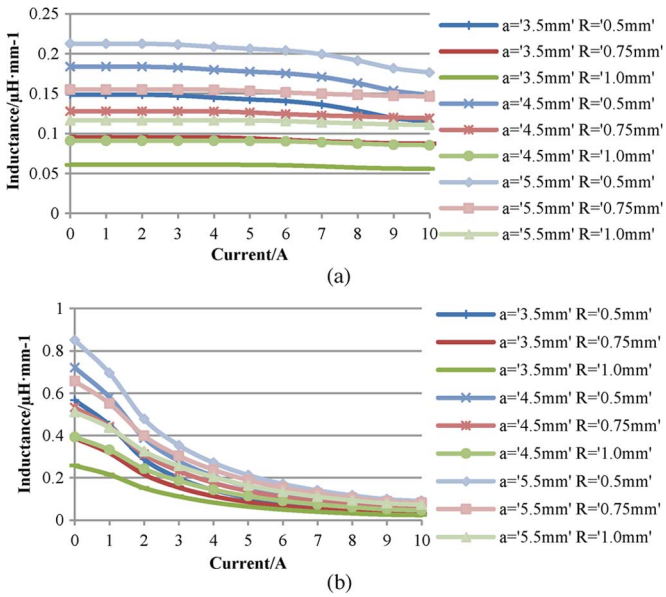

Fig. 11. Inductance versus load current. (a) $\mu_r = 50$. (b) $\mu_r = 200$.

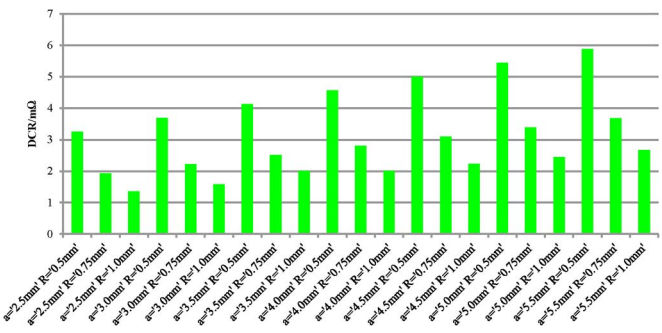

Fig. 12. DCR of the inductor.

Fig. 12 shows the calculated results of the DCR according to (7). With the increase in side length, the DCR of the inductor gradually increases, but for a certain side length, the DCR has a decreasing trend with the increase in radius.

By compromising the inductance values and DCR, $a = 4.5$ mm and $R = 0.75$ mm are selected in this design. Substituting inductance values into (6) yields thicknesses of each permeability. In this design, the thicknesses of $\mu_r = 50$ and $\mu_r = 200$ ferrite tapes are 2 and 1 mm, respectively. The whole core size is thus 18 mm × 18 mm × 3 mm. Inductances are 0.8 μH at 0 A and 0.3 μH at 10 A. DCR is thus 3.1 mΩ. Table I lists the coupling coefficients of the nine-window inductor obtained through the model and simulation. These coupling coefficients are obtained under the assumption that the windows are evenly

TABLE I
COUPLING COEFFICIENTS IN THE SIMULATED NINE-WINDOW INDUCTOR

	μ_r	$K_{pi\text{-}12}$	$K_{pi\text{-}13}$	$K_{pi\text{-}22}$	$K_{pi\text{-}23}$
Model	50	-0.166	0.121	0.126	-0.234
	200	-0.134	0.097	0.102	-0.214
Simulation	50	-0.173	0.131	0.145	-0.255
	200	-0.138	0.104	0.111	-0.234

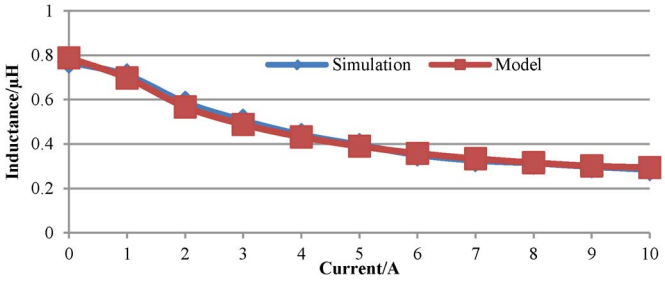

Fig. 13. Total inductances based on the model and the simulation.

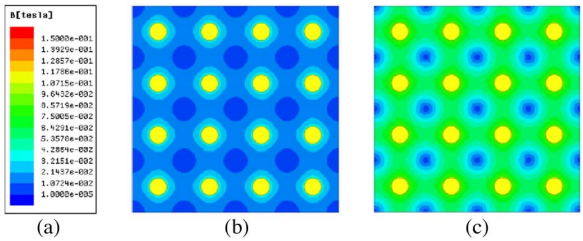

Fig. 14. Flux density distribution of 40 010 ($\mu_r = 50$). (a) Linear scale of flux density. (b) Flux density at 3-A load current. (c) Flux density at 10-A load current.

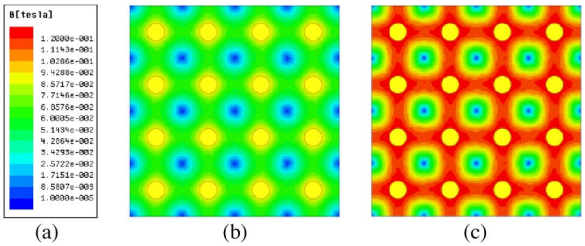

Fig. 15. Flux density distribution of 40 011 ($\mu_r = 200$). (a) Linear scale of flux density. (b) Flux density at 3-A load current. (c) Flux density at 10-A load current.

distributed on the magnetic core. Slight position offset of windows will introduce some error in the coupling coefficients. However, it will not have too much effect on the inductance value as long as the whole magnetic core area is fixed. This is because the reduction of coupling flux in one direction is generally compensated by the increase in coupling flux from other directions. Fig. 13 shows the inductance curves. The error between the model and the simulation is very small.

The flux density distributions of the nonlinear inductor at light load 3-A load current and 10-A load current for different permeability magnetic materials are illustrated in Figs. 14 and 15. The saturation flux density for 40 010 is about 150 mT, whereas

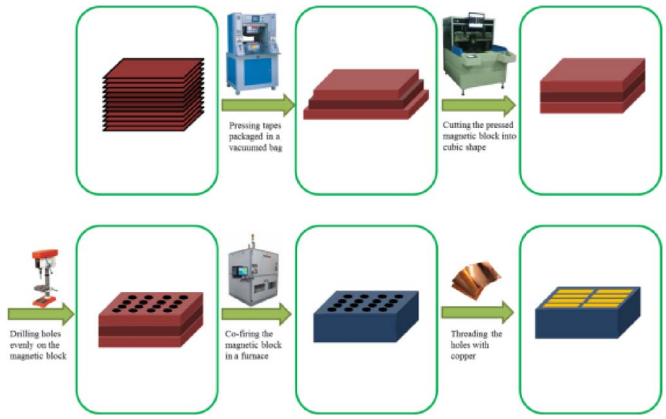

Fig. 16. Fabrication process of the 16-window two-permeability nonlinear inductor.

the saturation flux density for 40 011 is about 120 mT. For low-permeability magnetic material 40 010, the magnetic material has almost no saturation even at 10-A load current, resulting in nearly constant inductance value across the whole load range. However, for high-permeability magnetic material 40 011, the magnetic materials around the conductor have got saturated, leading to the gradual inductance drop across the whole load range.

IV. PROTOTYPE AND EXPERIMENT

The previous section has demonstrated the process of designing a 16-window two-permeability square-shaped nonlinear inductor. The inductance curve obtained through the model correlates very well with that obtained through complete FEA simulation. In this section, an LTCC nonlinear inductor prototype will be made according to above designing results.

Before the fabrication process, ferrite tapes should be first chosen from the manufacturers. The ferrite tapes used in this paper are from an LTCC tape provider ElectroScience. Two kinds of ferrite tapes are chosen for use. One is 40 010 whose permeability is about 50 after co-firing (the permeability can vary depending on peak co-firing temperature); the other is 40 011 whose permeability is about 200 after co-firing (the permeability can vary depending on peak co-firing temperature). The tapes are only about 70 μm thick, and they will shrink in the XY-direction and in the Z-direction during the co-firing process. Since 40 010 and 40 011 have different shrinking coefficients in the XY-direction, it will cause crack problem during the co-firing process if they are laminated directly. To avoid this issue, a sandwich structure is used, in which the low-permeability 40 010 layers are divided into two groups (the top layer and the bottom layer) and 40 011 were inserted between them before lamination. This symmetrical structure can effectively solve TEC mismatching of different materials without changing the electrical performances.

The fabrication process can be summarized in the following steps as shown in Fig. 16.

a) Cut the tapes into small pieces with the size of 30 mm × 30 mm. Among them are 40 pieces of 40 010, which are divided into two groups averagely and 20 pieces of 40 011.

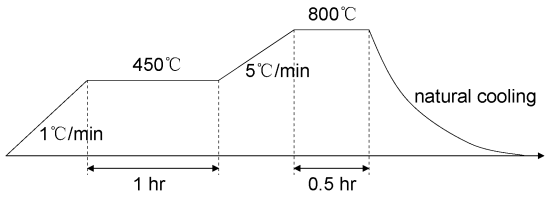

Fig. 17. Temperature profile of co-firing.

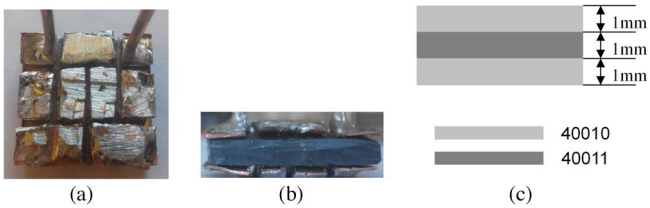

Fig. 18. Sixteen-window two-permeability ($a = 4.5$ mm, $R = 0.75$ mm). (a) Picture of the prototype. (b) Side view. (b) Magnetic core structure.

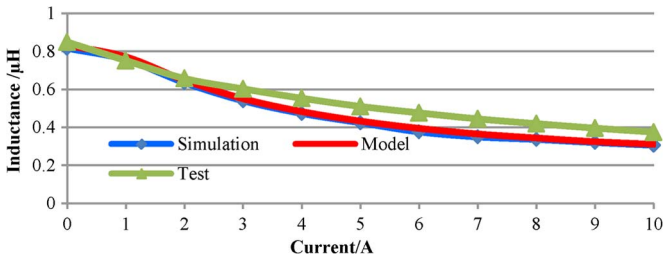

Fig. 19. Inductance curve based on modeling, simulation, and test.

b) Put the tapes in the sandwich structure (20 pieces of 40 010 on the top and 20 pieces of 40 010 at the bottom, between them are 20 pieces of 40 011) and conceal them in a vacuum plastic bag.
c) Put the plastic bag in a hydraulic press machine to press different layers into an integrated block under 1500 lbf/in^2.
d) Cut the four edges of the block to make sure that the block has 18 mm $\times$ 18 mm size after co-firing (the 17% shrinkage coefficient in the XY-direction should be taken into consideration; the size before is thus 21.06 mm $\times$ 21.06 mm before co-firing).
e) Drill 16 windows on the block evenly and make sure that the diameter is also 4.5 mm after co-firing (the shrinkage of the window size should be taken into consideration).
f) Put the block into the furnace and co-fire it according to the temperature profile shown in Fig. 17.
g) Solder copper wire and plate on the magnetic core to form the winding of the inductor.

A 16-window two-permeability nonlinear prototype is manually made by following the above described process. Pictures and structure of the prototype are shown in Fig. 18. For mass production, the last two steps can be combined into one step. Instead of using a copper plate, copper paste can be used to form the winding on the core, and they are put into the furnace for co-firing in nitrogen atmosphere. The inductor is composed of three layers. The top layer and the bottom layer are 1-mm-thick low-permeability magnetic material ($\mu_r = 50$), whereas the middle layer is 1-mm-thick high-permeability magnetic material ($\mu_r = 200$). The total height of the inductor is thus 3 mm.

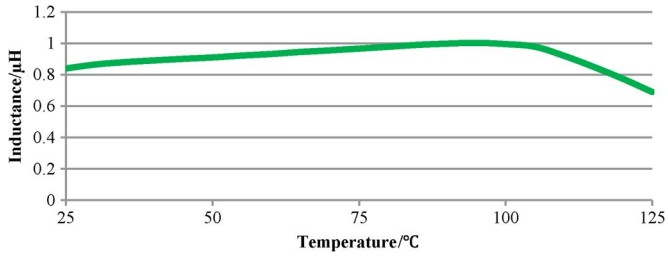

Fig. 20. Inductance value versus temperature.

Fig. 21. Picture of the chip inductor.

TABLE II
PARAMETERS OF THE TWO INDUCTORS

Items	DCR (mΩ)	Inductance (μH)	Volume (mm^3)	Mass (g)
Chip inductor	2.5	0.3	333	1.88
Nonlinear inductor	2.5	0.37~0.84	1000	3.65

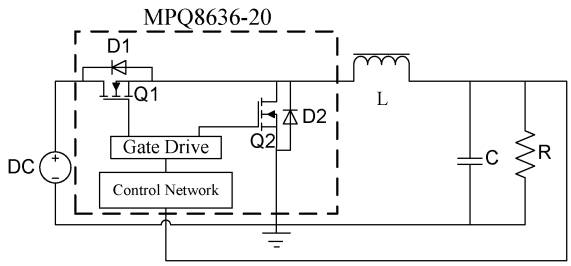

Fig. 22. Schematic of the buck converter for testing inductors.

TABLE III
PARAMETERS OF THE CONVERTER FOR EVALUATING THE INDUCTORS

Input Voltage	12 V
Output Voltage	3.3 V
Switching Frequency	1.5 MHz
Input capacitor	66 μF
Output capacitor	235 μF

The inductance curve of the prototype is obtained by measuring the current ripple amplitude and the off time in a 12-V-input 3.3-V-output buck converter. The result is illustrated in Fig. 19 to compare with the results obtained through the model and complete simulation. It can be observed that the proposed

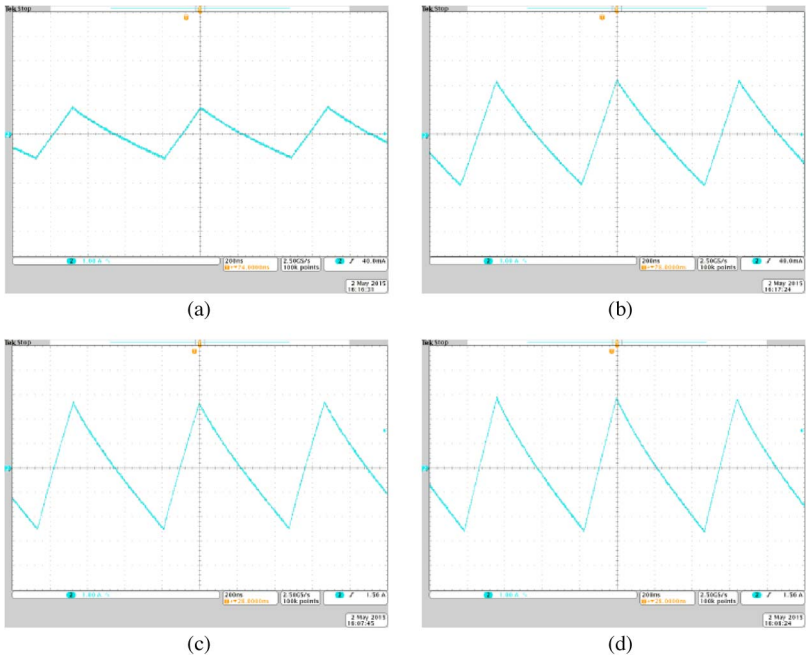

Fig. 23. Current ripple of the inductors (1 A/div). (a) Nonlinear inductor, 1-A load current. (b) Nonlinear inductor, 10-A load current. (c) Chip inductor, 1-A load current. (d) Chip inductor, 10-A load current.

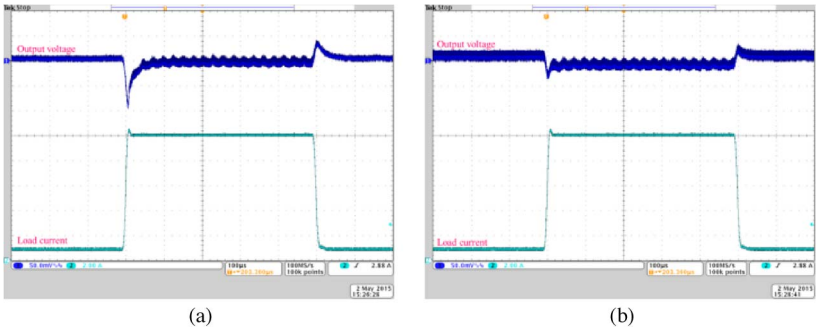

Fig. 24. Dynamic responses (CH1 50 mV/div and CH2 2 A/div). (a) Nonlinear inductor. (b) Chip inductor.

model correlates very well with the simulation. However, some differences exist between the modeling/simulation and the prototype test results. There are two reasons for this error. First, the prototype is manually made; the position of the windows is not precisely drilled on the substrate as in the simulation and modeling. Second, the B–H curve of the prototype is nonideal, which will introduce some inconsistency between the measurement and simulation. However, the error introduced by the B–H curve does not mean the accuracy of the model itself will be affected since the inductance curve obtained by the model correlates very well with the inductance curve obtained by the complete simulation. Inductance versus temperature is also measured with a thermal coupler. The result is illustrated in Fig. 20. The inductance value first rises to 1 μH at 85 °C from 0.84 μH at 25 °C, and then it drops to 0.7 μH at 125 °C.

The nonlinear inductor is used in a dc/dc converter to evaluate its performance of light load efficiency improvement. A chip inductor with nearly the same DCR and full-load inductance value is also selected to do an efficiency comparison. A picture of the chip inductor is shown in Fig. 21. Parameters of the chip inductor and the nonlinear inductor are listed in Table II. Both inductors are tested in a dc/dc converter designed based on an integrated buck regulator MPQ8636-20 from MPS [42]. The schematic of the converter is shown Fig. 22. Detailed information about the operating condition of the converter is shown in Table III. Current ripple of the inductors at 1- and 10-A load currents is shown in Fig. 23. Benefiting from the nonlinear characteristic, at 1-A load current, the current ripple of the nonlinear inductor is about 2-A peak–peak value, whereas that of the chip inductor is about 5.2-A peak–peak value. At 10-A load current, the current ripple of the nonlinear inductor becomes 4.2-A peak–peak value, whereas that of the chip inductor is about 5.3 A. Further test exposes that the inductance value of the nonlinear inductor still keeps about 0.28 μH even when the load current reaches 20 A. Dynamic responses of the nonlinear inductor and the chip inductor are also tested. Fig. 24 shows the dynamic response of the two inductors from 1- to 10-A current step. For the nonlinear inductor, the overshoot amplitude of is 50 mV, whereas the drop-off amplitude is larger, which is about 100 mV. For the chip inductor, both the overshoot amplitude and the drop-off amplitude are 40 mV. The current waveform of the nonlinear inductor at transient time is further

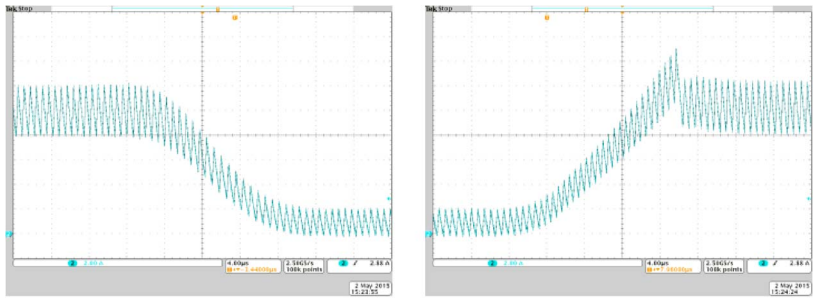

(a) (b)

Fig. 25. Current ripple change during dynamic transient (2 A/div). (a) Step-down. (b) Step-up.

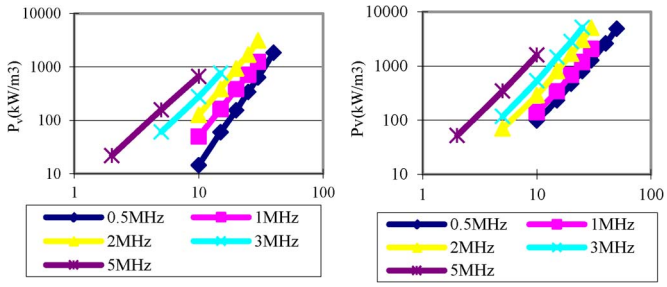

(a) (b)

Fig. 26. Power loss as a function of peak flux density with frequency as a parameter. (a) 40 010 ($\mu_r = 50$). (b) 40 011 ($\mu_r = 200$).

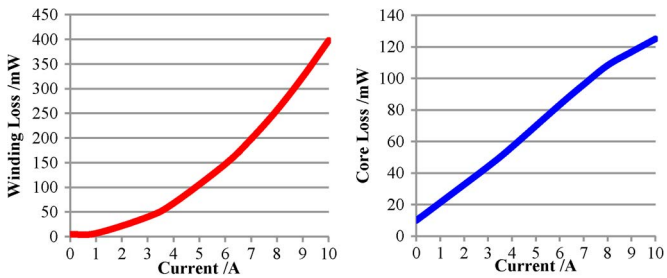

(a) (b)

Fig. 27. Loss of the nonlinear inductor. (a) Winding loss. (b) Core loss.

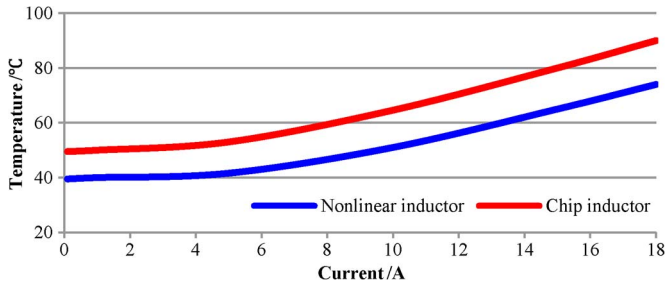

Fig. 28. Temperature of the nonlinear inductor and chip inductor versus load current.

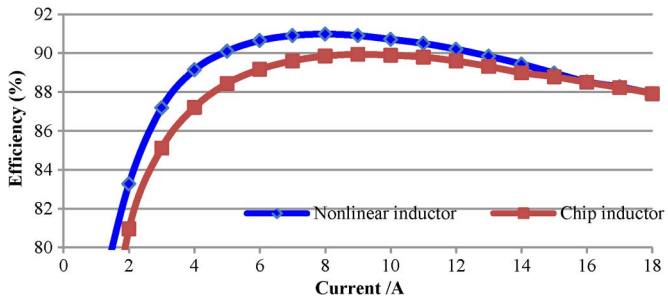

Fig. 29. Efficiency curves of the converter with the nonlinear inductor and the chip inductor.

shown in Fig. 25, in which the current ripple change is clearly illustrated to show the nonlinear characteristic of the inductor. A 3-D FEA simulation is further executed to calculate the core loss and winding loss of the designed inductor with Ansoft software. In the software, the algorithm for calculating the core loss is based on the classical Steinmetz equation, in which some coefficients should be extracted from the loss characteristics of the magnetic materials. Fig. 26 shows the measured core loss characteristic curves of the two kinds of magnetic materials. Fig. 27 shows the winding loss and core loss of the nonlinear inductor. With higher inductance value at light load, the nonlinear inductor is able to reduce the current ripple compared with the chip inductor, which, in turn, reduces the conduction loss of both the inductor and the power stage. Temperature of the nonlinear inductor and the chip inductor is measured in the same converter. As shown in Fig. 28, the nonlinear inductor has about 15 °C lower temperature than the chip inductor. Fig. 29 shows the efficiency curves of the converter with the two inductors. The nonlinear inductor can improve about 1.5% efficiency at light and intermediate loads.

V. Conclusion

This paper has focused on the design of a rectangle-shaped multiwindow multipermeability nonlinear inductor. A new model for inductance calculation has been derived. The proposed model significantly simplified the complicated FEA simulation of the nonlinear inductors by breaking down the inductor into three basic units. Instead of simulating the whole inductor, in the new model, a nine-window inductor, which is used to simulate the inductance of each unit by taking the coupling coefficients from adjacent windows into consideration, is used to obtain the inductance of each unit. The total inductance then can be obtained by multiplying the number of each unit with the corresponding inductance curve. The calculation results of the proposed model highly agree with the simulation results. A 16-window two-permeability inductor is designed to demonstrate the design process of such an inductor. The fabrication process is also illustrated during the prototype-making process. To verify the advantage of the nonlinear inductor, another chip inductor with nearly the same DCR and full-load inductance is also selected for comparison. Both inductors are

used in a dc/dc converter to test their performances. The results show the nonlinear inductor can improve the light load efficiency and maintain the same efficiency at full load.

REFERENCES

[1] E. Dallago, M. Passoni, and G. Venchi, "Analysis of high-frequency IGBT soft switching buck converter with saturable inductors," *IEEE Trans. Power Electron.*, vol. 22, no. 2, pp. 407–416, Mar. 2007.

[2] L. S. Fan and A. M. Khambadkone, "Nonlinear inductor design for improving light load efficiency of boost PFC," in *Proc. IEEE Energy Convers. Congr. Expo.*, 2009, pp. 1339–1346.

[3] K. Harada, H. Sakamoto, and K. Harada, "Saturable inductor commutation for zero voltage switching in DC–DC converter," *IEEE Trans. Magn.*, vol. 26, no. 5, pp. 2259–2261, Sep. 1990.

[4] R. Saito and S. Ushiki, "Reduced-resonant-current zero-voltage-switched forward converter with unsaturated-region resonance of saturable inductor," in *Proc. 13th INTELEC*, Nov. 5–8, 1991, pp. 151–158.

[5] J. A. Ferreira, A. Van Ross, and J. D. Van Wyk, "A generic soft switching converter topology with a parallel nonlinear network for high-power application," *IEEE Trans. Power Electron.*, vol. 7, no. 2, pp. 324–331, Apr. 1992.

[6] M. Stadler and J. Pforr, "Feed-forward control of non-linear inductors providing soft-switching of DC–DC-converters," in *Proc. Eur. Conf. Power Electron. Appl.*, Sep. 2–5, 2007, pp. 1–10.

[7] M. Stadler and J. Pforr, "Zero-voltage switched multi-phase converter utilizing nonlinear and coupled inductors," in *Proc. 22nd IEEE APEC*, Feb. 25–Mar. 1, 2007, pp. 1038–1042.

[8] J. M. Alonso and M. S. Perdigao, "Magnetic control of DC–DC resonant converters provides constant frequency operation," *IEEE Lett. Power Electron.*, vol. 46, no. 6, pp. 440–442, Mar. 2010.

[9] J. M. Alonso and M. A. D. Costa, "Investigation of a new control strategy for electronic ballasts based on variable inductor," *IEEE Trans. Ind. Electron.*, vol. 55, no. 1, pp. 3–10, Jan. 2008.

[10] S. T. S. Lee, H. S.-H. Chung, and S. Y. Hui, "Use of saturable inductor to improve the dimming characteristics of frequency-controlled dimmable electronic ballasts," *IEEE Trans. Power Electron.*, vol. 19, no. 6, pp. 1653–1660, Nov. 2004.

[11] L. Wang, Y. Pei, X. Yang, and Z. Wang, "Improving light and intermediate load efficiencies of buck converters with planar nonlinear inductors and variable on time control," *IEEE Trans. Power Electron.*, vol. 27, no. 1, pp. 342–353, Jan. 2012.

[12] M. H. Lim, J. D. Van Wyk, and Z. Liang, "Internal geometry variation of LTCC inductors to improve light-load efficiency of DC–DC converters," *IEEE Trans. Compon. Packag. Technol.*, vol. 32, no. 1, pp. 3–11, Mar. 2009.

[13] M. H. Lim, J. D. van Wyk, F. C. Lee, and K. D. T. Ngo, "A class of ceramic-based chip inductors for hybrid integration in power supplies," *IEEE Trans. Power Electron.*, vol. 23, no. 3, pp. 1556–1564, May 2008.

[14] R. Hahn, S. Krumbholz, and H. Reichl, "Low profile power inductors based on ferromagnetic LTCC technology," in *Proc. Electron. Compon. Technol. Conf.*, 2006, pp. 528–533.

[15] M. Mu, Y. Su, Q. Li, and F. C. Lee, "Magnetic characterization of low temperature co-fired ceramic (LTCC) ferrite materials for high frequency power converters," in *Proc. IEEE Energy Convers. Congr. Expo.*, 2011, pp. 2133–2138.

[16] Y. Su *et al.*, "Low profile LTCC inductor substrate for multi-MHz integrated POL converter," in *Proc. IEEE Appl. Power Electron. Conf. Expo.*, 2012, pp. 1331–1337.

[17] L. Wang, Y. Pei, X. Yang, and Z. Wang, "Design of ultrathin LTCC coupled inductors for compact DC/DC converters," *IEEE Trans. Power Electron.*, vol. 26, no. 9, pp. 2528–2541, Sep. 2011.

[18] M. H. Lim, J. D. van Wyk, and F. C. Lee, "Hybrid integration of a low-voltage, high-current power supply buck converter with an LTCC substrate inductor," *IEEE Trans. Power Electron.*, vol. 25, no. 9, pp. 2287–2298, Sep. 2010.

[19] Q. Li, Y. Dong, F. C. Lee, and D. Gilham, "High-density low-profile coupled inductor design for integrated point-of-load converters," *IEEE Trans. Power Electron.*, vol. 28, no. 1, pp. 547–554, Jan. 2013.

[20] Q. Li and F. C. Lee, "High inductance density low-profile inductor structure for integrated point-of-load converter," in *Proc. IEEE Appl. Power Electron. Conf. Expo.*, Feb. 2009, pp. 1011–1017.

[21] Y. Su, Q. Li, and F. C. Lee, "Design and evaluation of a high-frequency LTCC inductor substrate for a three-dimensional integrated DC/DC converter," *IEEE Trans. Power Electron.*, vol. 28, no. 9, pp. 4354–4364, Sep. 2013.

[22] TI Products, LMZ10501, Texas Instruments, Dallas, TX, USA, 2014. [Online]. Available: http://www.ti.com/lit/ds/symlink/lmz10501.pdf

[23] TI Products, LMZ10500, Texas Instruments, Dallas, TX, USA, 2015. [Online]. Available: http://www.ti.com/lit/ds/symlink/lmz10500.pdf

[24] Murata μModule Products. [Online]. Available: http://power.murata.com/en/products/micro-dc-dc.html

[25] Z. Liu, A. Abou-Alfotouh, and M. Wilkowski, "Nonlinear inductor modeling for power converter," in *Proc. 27th IEEE APEC*, Feb. 5–9, 2012, pp. 1868–1871.

[26] R. A. Salas and J. Pleite, "Nonlinear inductance calculations of a ferrite inductor with a 2D finite element model," in *Proc. ICEAA*, Sep. 12–16, 2011, pp. 986–989.

[27] G. K. Stefopoulos, G. J. Cokkinides, and A. P. S. Meliopoulos, "Quadratized model of nonlinear saturable-core inductor for time-domain simulation," in *Proc. IEEE PES Gener. Meet.*, Jul. 26–30, 2009, pp. 1–8.

[28] J. H. B. Deane, "Modeling the dynamics of nonlinear inductor circuits," *IEEE Trans. Magn.*, vol. 30, no. 5, pp. 2795–2801, Sep. 1994.

[29] A. Stadler, C. Gulden, and T. Stolzke, "Nonlinear inductors for active power factor correction circuits," in *Proc. 15th Int. EPE/PEMC*, Sep. 4–6, 2012, pp. LS7b-2.1-1–LS7b-2.1-4.

[30] T. M. Andersen *et al.*, "Modeling and Pareto optimization of microfabricated inductors for power supply on chip," *IEEE Trans. Power Electron.*, vol. 28, no. 9, pp. 4422–4430, Sep. 2013.

[31] L. Qu and P. L. Chapman, "Extraction of low-order non-linear inductor models from a high-order physics-based representation," *IEEE Trans. Power Electron.*, vol. 21, no. 3, pp. 813–817, May 2006.

[32] G. Zhu, B. McDonald, and K. Wang, "Modeling and analysis of coupled inductors in power converters," *IEEE Trans. Power Electron.*, vol. 26, no. 5, pp. 1355–1363, May 2011.

[33] J.-L. Kotny, X. Margueron, and N. Idir, "High-frequency model of the coupled inductors used in EMI filters," *IEEE Trans. Power Electron.*, vol. 27, no. 6, pp. 2805–2812, Jun. 2012.

[34] S. Raju, R. Wu, M. Chan, and C. P. Yue, "Modeling of mutual coupling between planar inductors in wireless power applications," *IEEE Trans. Power Electron.*, vol. 29, no. 1, pp. 481–490, Jan. 2014.

[35] J. M. Lopera, M. J. Prieto, A. M. Pernia, and F. Nuno, "A multiwinding modeling method for high frequency transformers and inductors," *IEEE Trans. Power Electron.*, vol. 18, no. 3, pp. 896–906, May 2003.

[36] D. Maksimovic, R. W. Erickson, and C. Griesbach, "Modeling of cross-regulation in converters containing coupled inductors," *IEEE Trans. Power Electron.*, vol. 15, no. 4, pp. 607–615, Jul. 2000.

[37] J. Qiu and C. R. Sullivan, "Design and fabrication of VHF tapped power inductors using nanogranular magnetic films," *IEEE Trans. Power Electron.*, vol. 27, no. 12, pp. 4965–4975, Dec. 2012.

[38] S. S. M. Chan, H. S.-H. Chung, and Y. S. Lee, "Design and implementation of dimmable electronic ballast based on integrated inductor," *IEEE Trans. Power Electron.*, vol. 22, no. 1, pp. 291–300, Jan. 2007.

[39] D. Kimhi and S. Ben-Yaakov, "A SPICE model for current mode PWM converters operating under continuous inductor current conditions," *IEEE Trans. Power Electron.*, vol. 6, no. 2, pp. 281–286, Apr. 1991.

[40] J. Lu *et al.*, "Modeling, design, and characterization of multiturn bondwire inductors with ferrite epoxy glob cores for power supply system-on-chip or system-in-package applications," *IEEE Trans. Power Electron.*, vol. 25, no. 8, pp. 2010–2017, Aug. 2010.

[41] M. Xu, J. Zhou, K. Yao, and F. C. Lee, "Small signal modeling of a high bandwidth voltage regulator using coupled inductors," *IEEE Trans. Power Electron.*, vol. 22, no. 2, pp. 399–406, Mar. 2007.

[42] MPQ8636-20 datasheet, 2015. [Online]. Available: http://www.monolithicpower.com/

Laili Wang (S'07–M'13) was born in Shaanxi Province, China, in 1982. He received the B.S., M.S., and Ph.D. degrees from Xi'an Jiaotong University, Xi'an, China, in 2004, 2007, and 2011, respectively, all in electrical engineering.

Since 2011, he has been a Postdoctoral Research Fellow with the Department of Electrical and Computer Engineering, Queen's University, Kingston, ON, Canada. His research focuses on the packaging and integration of passive devices in high-frequency high-power-density dc/dc converters.

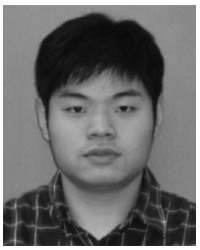

Yajie Qiu (S'13) received the M.Sc. degree from Anhui University of Technology, Ma'anshan, China, in 2011. He is currently working toward the Ph.D. degree in electrical engineering at Queen's University, Kingston, ON, Canada.

He holds one pending U.S. patent. His research interests include topologies and control methods for ac–dc converters with power factor correction and LED drivers, nonlinear control to achieve fast dynamic performance for dc–dc converters, and modulation schemes for resonant converters.

Mr. Qiu was a recipient of the Outstanding Presentation Award at the 2015 IEEE Applied Power Electronics Conference and Exposition and the Conference Travel Award from the Power Sources Manufacturers Association.

Hongliang Wang (M'12) received the B.Sc. degree from Anhui University of Science and Technology, Huainan, China, in 2004 and the Ph.D. degree from Huazhong University of Science and Technology, Wuhan, China, in 2011.

From July 2004 to May 2005, he was an Electrical Engineer with the Zhejiang Hengdian Thermal Power Plant. From June 2011 to May 2013, he was a Senior System Engineer with Sungrow Power Supply Company, Ltd. Since May 2013, he has been a Postdoctoral Fellow with the Department of Electrical and Computer Engineering, Queen's University, Kingston, ON, Canada. He holds 36 China patents and seven pending U.S. patents. His research interests include photovoltaics, uninterruptible power supplies, microgrids, resonant converters, and LED drivers.

Dr. Wang has been a member of the Technical Committee on Renewable Energy Power Conversion within the China Power Supply Society since September 2013 and of the Technical Committee on Standardization within the China Power Supply Society since July 2014.

Zhiyuan Hu (S'10–M'14) received the M.Sc. degree from the University of Ottawa, Ottawa, ON, Canada, in 2010 and the Ph.D. degree in electrical engineering from Queen's University, Kingston, ON, in 2014.

From 2007 to 2010, he was with Potentia Semiconductor Corporation and Power Integrations Inc., working in the area of reference design and IC validation for power management ICs. He holds one pending U.S. patent. His research interests include resonant converters, digital control, digital communication for isolated power supplies, and power factor correction.

Dr. Hu received conference travel awards as a student from the IEEE Industry Applications Society and IEEE Power Electronics Society and the Power Sources Manufacturers Association.

Yan-Fei Liu (M'94–SM'97–F'13) received the Ph.D. degree from Queen's University, Kingston, ON, Canada, in 1994.

From February 1994 to July 1999, he was a Technical Advisor with the Advanced Power System Division, Nortel Networks. In 1999, he joined Queen's University, where he is currently a Professor with the Department of Electrical and Computer Engineering. He holds 22 U.S. patents and has published more than 130 technical papers in IEEE TRANSACTIONS and conference proceedings. He is also a principal contributor to two IEEE standards. His research interests include digital control technologies for high-efficiency fast-dynamic-response dc–dc switching converters and ac–dc converters with power factor correction, resonant converters and server power supplies, and LED drivers.

Prof. Liu serves as Chair of the IEEE Power Electronics Society Technical Committee on Power Conversion Systems and Components and served as Technical Program Cochair for the 2011 IEEE Energy Conversion Congress and Exposition. He has been also serving as an Associate Editor for the IEEE TRANSACTIONS ON POWER ELECTRONICS since 2001 and the Editor-in-Chief for the Special Issue of Power Supply on Chip of the IEEE TRANSACTIONS ON POWER ELECTRONICS.